

Simulation of aluminum alloy flowing in friction stir welding with a multiphysics field model

Jian Luo¹ · Shixian Li¹ · Wei Chen¹ · Junfeng Xiang¹ · Hong Wang¹

Received: 10 November 2014 / Accepted: 26 April 2015 / Published online: 7 May 2015
© Springer-Verlag London 2015

Abstract The three-dimensional model for friction stir welding was established by coupling thermal, force, and flowing fields. The weld shape, surface stripes, weld defect, temperature field, and material flow behavior were predicted. The transient heat transfer phenomenon and material mixing pattern at the stir zone was primarily studied. The material flow mechanism was investigated. The experimental results strongly supported the reliability and accuracy of the model and simulation. The rotational speed to welding speed ratio R_{ω}/U_w plays an important role in transient heat transfer, temperature field, velocity field, material mixing pattern, and weld defect appearance.

Keywords Multiphysics field · Friction stir welding · Fluid mechanics · Mixing pattern · Surface stripes

1 Introduction

Friction stir welding (FSW) is widely accepted to be one of the most significant welding techniques that emerged in the last 20 years. It is a solid-state joining process in which a rotating tool with a shoulder and a threaded pin moves along the butt surfaces of two rigidly clamped workpieces placed on a back-plate [1, 2]. FSW was developed for joining difficult-to-weld Al-alloys and has been implemented by industry in the manufacturing of several products [3]. Material flow behavior

is crucial for obtaining a sound FSW joint. Due to the complexity of modeling material flow (accompanied with large plastic deformation), how to characterize material flow has always been a hot topic as well as difficult work. Several approaches to FSW simulation were discussed in literature [4–17]. Schmidt et al. [4] developed a fully coupled thermo-mechanical three-dimensional FE model to analyze the primary conditions under which the cavity behind the tool is filled. Sonne et al. [5] implemented a numerical model consisting of a heat transfer analysis and a sequentially coupled quasi-static stress analysis to study the effect of the hardening law on the residual stresses as well as on the final yield stress. Carlone et al. [6] used a CFD model to simulate material flow and temperature distribution in FSW. Smith et al. [7] used the Arbitrary Lagrangian Eulerian technique to show promising simulation and predict defect formation. The effects of the contact boundary conditions on material flow mechanism were studied by Ulysse [8]. Deng and Xu [9] adopted solid mechanics-based two-dimensional finite element models and computational procedures to simulate material flow process. Colegrove et al. [10] applied the computational fluid dynamics code FLUENT to model the three-dimensional (3D) material flow. Heurtier et al. [11] introduced a semi-analytical model based on the velocity fields typically used in fluid mechanics and incorporating heat input from the tool shoulder and the plastic strain of the bulk material. Zhang et al. [12] built a 3D model to simulate material flow under different parameters based on the nonlinear continuum mechanics and obtained quasi-linear relation between axial load on the shoulder and equivalent plastic strain. Nandan et al. [13] used the 3D non-Newtonian viscoplastic flow model to visualize the primary mechanism of material flow. An Eulerian thermo-mechanical coupled modeling for the FSW was proposed by Jacquin et al. [14], who considered the velocity fields as convective when describing material flow. Zhang et al. [15] developed

✉ Jian Luo
luojian2007@gmail.com

¹ State Key Laboratory of Mechanical Transmission, College of Automotive Technology, Chongqing University, Chongqing 400030, People's Republic of China

analytical models to estimate the peak temperature and grain size in the nugget zone. Zhang et al. [16] established a new Eulerian model based on solid mechanics to study material flow, slipping velocity, and torque during friction stir welding process. Al-Badour et al. [17] developed a thermo-mechanical finite element model based on coupled Eulerian Lagrangian method to simulate friction stir welding using different tool pin profiles.

The present investigation was conducted to develop a complete model description of heat generation and material flow during FSW. An advanced semi-analytical approach with a moving coordinate system was introduced to describe the material flow around the tool, which was derived from the original formulations proposed by Heurtier et al. [11] and improved by combining with Jacquin's principle for whole or partially sticking/sliding conditions. A 3D coupled thermo-mechanical model based on fluid mechanics was introduced to simulate the FSW process. The COMSOL Multiphysics tool has been employed due to its flexibility and adaptability in solving coupled multiphysics field problem. The model was verified by comparing the weld shape, surface stripes, peak temperature, and material flow behavior in experimental and simulation conditions. The model can be used to predict heat transfer and mixing patterns for FSW process under certain process parameters.

2 Models

A 3D multiphysics field finite element model including heat transfer, material flow, and structure mechanics was established. A moving coordinate system fixed on the friction tool was employed to simplify the process. The frictional heat at the workpiece-tool interface and plastic deformation heat were involved in the heat source.

2.1 Assumptions

Assumptions and initial considerations were made as follows:

1. The tool pin was assumed to be a cylinder with no thread. The model only investigated the stable welding process, so the plunging process was not considered;
2. The aluminum workpiece has infinite length, which means that the analysis neglected the edge effect of the workpiece;
3. The friction coefficient above the melting temperature of the workpiece was set to zero;
4. A moving coordinate system was also adopted to establish the heat transfer and material flow coupled model, so the transient heat transfer problem became a quasi-steady convection-conduction problem that was compliant to model.

5. A single block continuum model (block sheet with a gap), as suggested by Buffa et al. [18], was introduced to avoid contact instabilities due to the intermittent contact at the sheet/sheet interfaces.

2.2 Heat transfer

The description of temperature distribution was based on a quasi-steady heat transfer equation, which considered only the temperature as the dependent variable.

1. Heat transfer governing equation: A quasi-steady heat transfer approach was introduced to obtain the temperature distribution, which was continuous in time but moving with given constant velocity by the introduction of welding speed in the heat transfer equation. The 3D quasi-steady governing equation in a moving coordinate system can be described as:

$$\rho \cdot C_p \cdot \vec{U} \cdot \nabla T = \nabla \cdot (\kappa \cdot \nabla T) + Q \quad (1)$$

where ρ is the density (kg/m^3), C_p is the heat capacity (J/(kg K)), κ is the thermal conductivity (W/(m K)), and Q is the heat source (W/m^3). To improve the calculation precision, ρ , C_p , and κ of the 6061-T651 aluminum alloy are temperature-dependent functions, which were given in the form of quadratic polynomials according to Zhang et al. [19].

2. Heat generation: Previous studies only considered the heat generated by the friction of the shoulder, but ignored the heat from other sources. The heat generation includes: (a) the friction heat at the shoulder/workpiece interface and (b) the friction heat at the pin/workpiece interface and internal heat generation.

1. Friction heat input at the interface between tool shoulder and workpiece:

The heat input at the interface between the tool shoulder and the workpiece q_{shoulder} can be expressed as:

$$q_{\text{shoulder}} = \begin{cases} \mu \cdot U_w \cdot (2\pi r R_{\omega/U_w}) \cdot \frac{F_n}{60A_s} & ; T < T_{\text{melt}} \\ 0 & ; T \geq T_{\text{melt}} \end{cases} \quad (2)$$

where μ is the frictional coefficient, U_w is the welding speed (mm/min), r is the cylindrical coordinate, R_{ω/U_w} is the ratio of rotational speed to welding speed, F_n is the axial force (N), A_s is the contact area of the shoulder (mm^2), and T_{melt} is the melting point (K). This expression was defined by the local heat flux per unit area (W/m^2) at the distance r from the

center axis of the tool. The temperature-dependent friction coefficient μ can be approximately described by a piecewise linear equation by Zhang et al. [19]:

$$\mu = \mu_0 - f_0(T-273) \quad (3)$$

where

$$f_0 = \begin{cases} -2.27 \times 10^{-3} & , 273 < T < 423 \\ 2.54 \times 10^{-3} & , 423 < T < 533 \\ 5.94 \times 10^{-3} & , 533 < T < 873 \end{cases} \quad (4)$$

$$\mu_0 = \begin{cases} 0.18 & , 273 < T \leq 423 \\ 0.90 & , 423 < T \leq 533 \\ 0.36 & , 533 < T \leq 873 \end{cases} \quad (5)$$

The real function of the frictional coefficient was taken as a piecewise function depended on temperature:

$$\begin{aligned} \mu = & (0.18 + (2.27e-3)*(T-273))*((T > 273)*(T < 423)) \\ & + (0.90 - (2.54e-3)*(T-273))*((T > 423)*(T \leq 530)) \\ & + (0.36 + (5.94e-4)*(T-273))*((T > 533)*(T \leq 873)) \end{aligned} \quad (6)$$

So the heat input of the shoulder Q_{shoulder} can be calculated by:

$$r_p Q_{\text{shoulder}} = \int_0^{2\pi} \int_{r_p}^{r_s} q_{\text{shoulder}} \cdot r \cdot dr \cdot d\theta \quad (7)$$

where r and θ are the cylindrical coordinates.

- Heat input from the friction at the tool pin / workpiece interface and internal heat generation: The description of two different kinds of heat generating sources was required: the pin friction heat and the internal heat generation. The internal heat generation was derived from material plastic deformation heat. About 90 % of the plastic deformation was assumed to be converted into heat. The term of heat generation rate can be expressed as the product of the effective stress and effective strain-rate [8]. A complete solution existed between the two heat sources. The two heat sources were coupled using the following form [4]:

$$Q_{\text{pin}} = \frac{2\mu k \bar{Y}(T) \pi r_p h V_{rp}}{\sqrt{3(1+\mu^2)}} + \frac{2}{3} \pi r_p h k \bar{Y}(T) V_m \quad (8)$$

where Q_{pin} is the heat source of the pin, $\bar{Y}(T)$ is temperature-dependent yield stress, is the radius of the tool pin, h is the thickness of the workpiece, V_{rp} is the velocity of the pin, and V_m is the material flow speed. In this work, the temperature-dependent

Table 1 Yield stress depended on temperature of 6061-T6 aluminum alloy [20]

Temperature (K)	311	366	394	422	477	533	589	644
Yield stress (MPa)	241	232	223	189	92	34	34	12

conductivity and specific heat coefficients for 6061-T6 aluminum alloys were adopted. The Eq. (8) did not consider the heat input related to the thread profile of the pin. A smooth cubic interpolating curve is defined in Table 1.

- Boundary and initial conditions: The heat continuity condition was applied to the surface of two aluminum workpiece. The boundary and initial conditions are shown in Fig. 1. Since the tool's rotational speed was far greater than the welding speed, the relative speed moving between the tool, and workpiece materials from the advancing to the retreating side should have little variation. In order to simplify the model and reduce calculation time, the contact surface between the adjoining sheets was assumed to be a symmetry surface.

The details of the boundary conditions and the initial condition are listed as follows:

Surface 1 is the heat dissipation of natural convective cooling and radiation:

$$-\vec{n} \cdot (-\kappa \cdot \nabla T) = h_u(T_0 - T) + \varepsilon \sigma (T_0^4 - T^4) \quad (9)$$

where \vec{n} is the normal vector, h_u is the convection coefficient at surface 1, ε is the emissivity, and σ is the Stefan Boltzmann's constant.

Convective cooling exists through the contact between surfaces 2, 3, and 4 and the retaining plates:

$$-\vec{n} \cdot (-\kappa \cdot \nabla T) = h_b(T_0 - T) \quad (10)$$

where h_b is the convection coefficient at surfaces 2, 3, and 4.

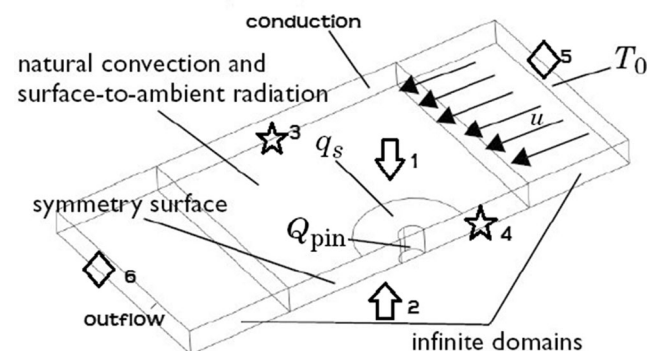


Fig. 1 Boundary and initial conditions of numerical model

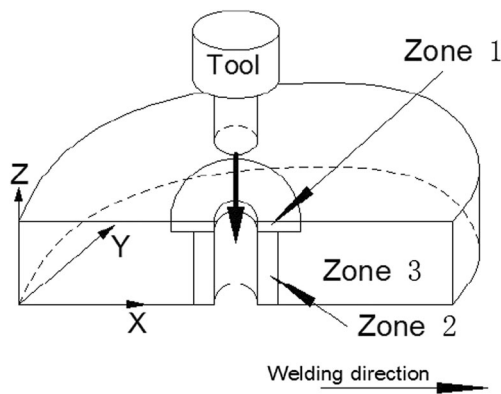


Fig. 2 Material flow model of the FSW

Surface 5 has a constant ambient temperature set as:

$$T_0 = 300 \text{ K} \quad (11)$$

Surface 6 is the outflow boundary:

$$\vec{n} \cdot (-\kappa \cdot \nabla T) = 0 \quad (12)$$

2.3 Material flow

The semi-analytical dynamics model with a cylindrical coordinate system was applied. The material flow model was divided into three different zones according to the different flow patterns they experienced during welding, as shown in Fig. 2.

The velocity fields of the material flow were described as follows:

1. The velocity field of zone 1 (the plastic deformation zone generated by the interaction between the shoulder and the workpiece):

$$\vec{U}_1 = \begin{bmatrix} u \\ v \\ w \end{bmatrix} = \begin{bmatrix} U_w \left[\left(1 - \frac{r_p^2}{r^2} \cos 2\theta \right) - r \sin \theta \cdot \frac{\omega_p}{U_w} \cdot \frac{z_{\text{surface}} - z_{\text{bottom}}}{z_{\text{surface}} - z_{\text{flowarmb}}} \right] \\ U_w \left[\left(1 - \frac{r_p^2}{r^2} \sin 2\theta \right) + r \cos \theta \cdot \frac{\omega_p}{U_w} \cdot \frac{z_{\text{surface}} - z_{\text{bottom}}}{z_{\text{surface}} - z_{\text{flowarmb}}} \right] \\ 0 \end{bmatrix} \quad (13)$$

where z_{surface} is the coordinate of the workpiece upper surface in the z -coordinate direction, z_{bottom} is the

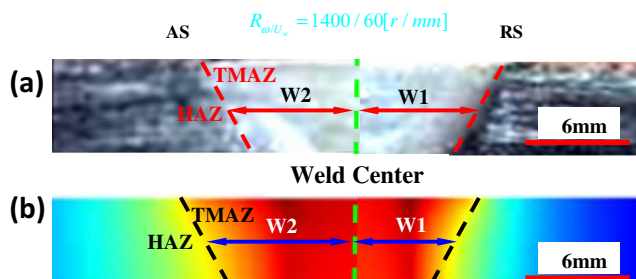


Fig. 3 FSW weld appearances from **a** experimental result and **b** simulation result

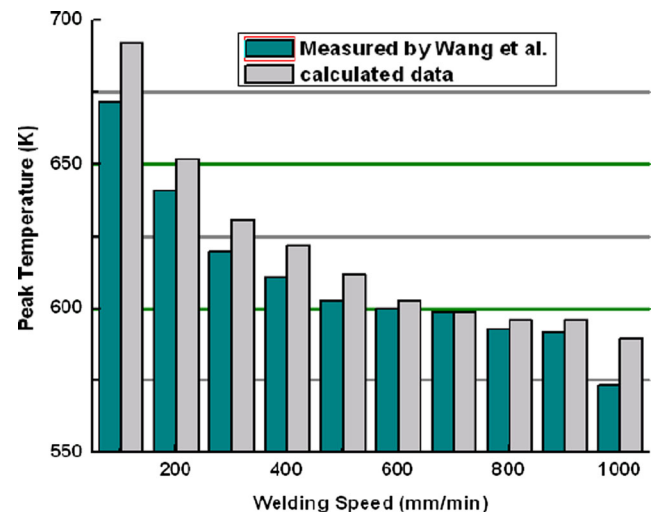


Fig. 4 Peak temperatures during FSW under different welding speeds

coordinate of workpiece bottom surface in the z -coordinate direction, and z_{flowarmb} is the coordinate of the “flow arm zone” bottom surface in the z -coordinate direction.

2. The velocity field of zone 2 (the nugget zone):

$$\vec{U}_2 = \begin{bmatrix} u \\ v \\ w \end{bmatrix} = \begin{bmatrix} U_w \left[\left(1 - \frac{r_p^2}{r^2} \cos 2\theta \right) - r \sin \theta \cdot \frac{\omega_p}{U_w} \cdot \frac{z_{\text{surface}} - z_{\text{bottom}}}{z_{\text{surface}} - z_{\text{flowarmb}}} \right] - \frac{1}{r} \cdot \frac{vz}{r^2 + z^2 - R_v} \cos \phi \\ U_w \left[\left(1 - \frac{r_p^2}{r^2} \sin 2\theta \right) + r \cos \theta \cdot \frac{\omega_p}{U_w} \cdot \frac{z_{\text{surface}} - z_{\text{bottom}}}{z_{\text{surface}} - z_{\text{flowarmb}}} \right] + \frac{1}{r} \cdot \frac{vz}{r^2 + z^2 - R_v} \sin \phi \\ - \frac{v}{r} \cdot \frac{\sqrt{r^2 - R_v}}{r^2 + z^2 - R_v} \end{bmatrix} \quad (14)$$

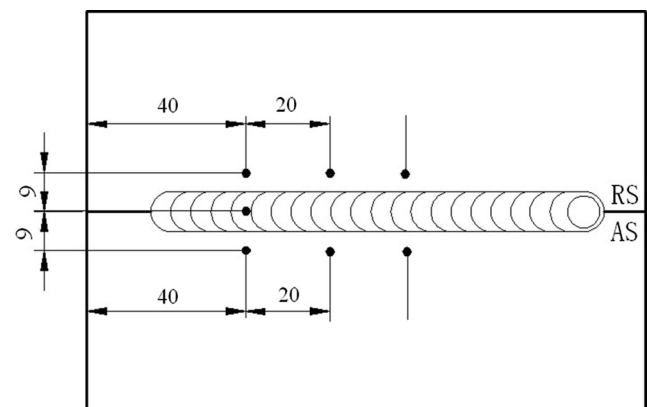
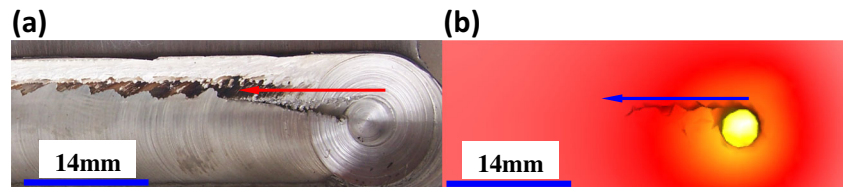


Fig. 5 Temperature measurement in FSW

Fig. 6 Weld defect in friction stir welding joints obtained from **a** experiment and **b** simulation



where v is the material flow velocity at 1 mm from vortex center, R_v is the position of the vortex center, and ϕ is the angle between the point projection and x -axis on the xy plane.

3. The velocity field of zone 3 (non-plastic deformation zone):

$$\vec{U}_3 = \begin{bmatrix} u \\ v \\ w \end{bmatrix} = \begin{bmatrix} U_\omega - \frac{1}{r} \cdot \frac{vz}{r^2 + z^2 - R_v} \cos\phi \\ \frac{1}{r} \cdot \frac{vz}{r^2 + z^2 - R_v} \sin\phi \\ -\frac{v}{r} \cdot \frac{\sqrt{r^2 - R_v}}{r^2 + z^2 - R_v} \end{bmatrix} \quad (15)$$

4. Boundary conditions:

The non-slip boundary condition was applied to all external boundaries (Fig. 1). The slip boundary condition was imposed to contact interfaces of zone 1/zone 2, zone 1/zone3, and zone 2/zone 3 (as shown in Fig. 2). The welding velocity was applied to all simulation domains. The actual material flow velocity was obtained by subtracting the overall velocity from the welding velocity. The manner in which the velocity and path correspond to the actual material flow was obtained through the following expression:

$$\vec{U}_R = (u_r, v_r, w_r) = \vec{U} - (U_w - U_w, w) \quad (16)$$

where \vec{U}_R is the superposition of welding velocity and the material flow velocity (mm/s).

3 The validation of the model

The temperature field, weld formation, velocity field, and defect were involved in the multiphysics field model of FSW. In

order to verify the validity and reliability of the multiphysics field model, the simulation results were compared with the corresponding experimental results. The tool geometry in the experiment and the simulation was identical. The tool pin was a cylinder without thread. The diameter of the pin was 6 mm. The diameter of the shoulder was 15 mm. The length of the pin was 5.8 mm. The tool material was H13 steel. The tilt angle was set to be 0° during welding. Two $160 \times 50 \times 5$ mm 6061-T6 aluminum alloy sheet was used as workpieces.

In order to compare the experimental result with the simulation result, the location of the boundaries between HAZ and TMAZ was defined at the temperature threshold of 350°C , which was based on the study of Lin et al. [21]. The width at the middle of the boundaries was regarded as a standard of comparison, as shown in Fig. 3. The average weld widths from the experiment and simulation were 14.3 and 15.6 mm, respectively. These data indicate that the weld shape obtained from simulation was in agreement with that of the experiment result under the same welding parameters. Figure 3 also shows two differences between the weld appearances obtained from experiment and simulation:

1. Profile difference: the edges of the weld cross section in the experiment (Fig. 3a) was convex at the middle; while the edges in the simulation (Fig. 3b) was concave at the middle, and the HAZ at AS and RS was not symmetrical about the weld center;
2. Weld width difference between RS (W1) and AS (W2): the W1 and W2 in the experiment were 6.9 and 7.4 mm, respectively; while the W1 and W2 in the simulation were 6.7 and 8.9 mm, respectively.

The new model of FSW was used to calculate the temperature field and the results were compared with the experimental results from the work of Wang et al. [22] by using the same

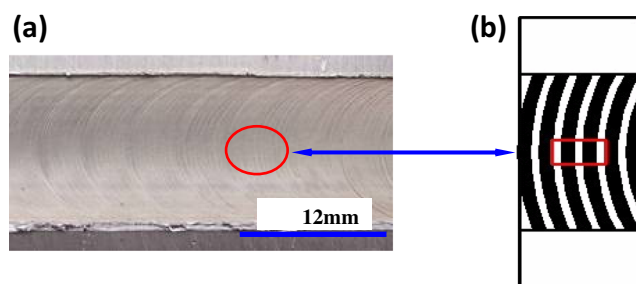


Fig. 7 Interval of surface stripes and curvature of arch lines on FSW joints: **a** experimental result and **b** simulation result

Table 2 Welding parameters for FSW simulation

No.	Parameter	Notation	Unit	Levels	
1	Rotational speed	n	rpm	950	1400
2	Welding speed	U_w	mm/min	40–100	100–700
3	Axial force	F_n	kN	8	9–19
4	Shoulder diameter	r_{shoulder}	mm	15	
5	Pin diameter	v_p	mm	6	
6	Pin length	l	mm	5.8	

welding parameters. Figure 4 shows a comparison between the calculated and measured peak temperature under a rotational speed of 950 r/min and an axial force of 9 kN.

In Fig. 4, compared with the experimental values measured by Wang et al. [22], the calculated values were slightly higher. There were large differences between the calculated and measured values when the welding speeds were 100 and 1000 mm/min. When the welding speed was from 600 to 800 mm/min, the calculated peak temperatures were approximately equal to the experimental results. This suggests that the model had small errors at low and high welding speeds, but agreed with the experiment results at moderate welding speeds.

The errors may be attributed to the different clamping conditions between the experiment and simulation. The simplified boundary conditions result in the decrease of convective cooling. When the welding speed was very high (1000 mm/min), the significantly higher temperature in the numerical model might be attributed to excessive heat generated by the increase of plastic strain, which was caused by the increase of flow stress. The increment of peak temperature increased with the decrease of welding speed. Such regularity existed in both

calculated and experimental results. Thus the proposed thermal-flow coupled model was valid and reliable.

Six points were selected on the workpieces to measure the temperature during FSW process using the platinum rhodium thermocouple. The ratio was 1400/400 r/mm, and the axial force was 18 kN. The measured points were distributed near the weld surface, as shown in Fig. 5. Under the same welding parameters, the measured average peak temperature was 643 K (according to Wang et al. [22]), while the calculated value was 672 K at the same position. Such similar results between calculation and experiment indicate that the model is effective.

Several defects appeared in the weld when improper R_w/U_w was used. Figure 6 shows a comparison of the surface weld defect between the experimental results and the simulation results under the same condition ($R_w/U_w = 1400/30$ r/mm). The simulation result coincided well with the experimental result. It suggests that the weld defect in FSW can be predicted by this coupled model.

The weld defect shown in Fig. 6 belongs to groove or tunnel defect. Researches show that such type of defects is mainly caused by improper welding parameters which result

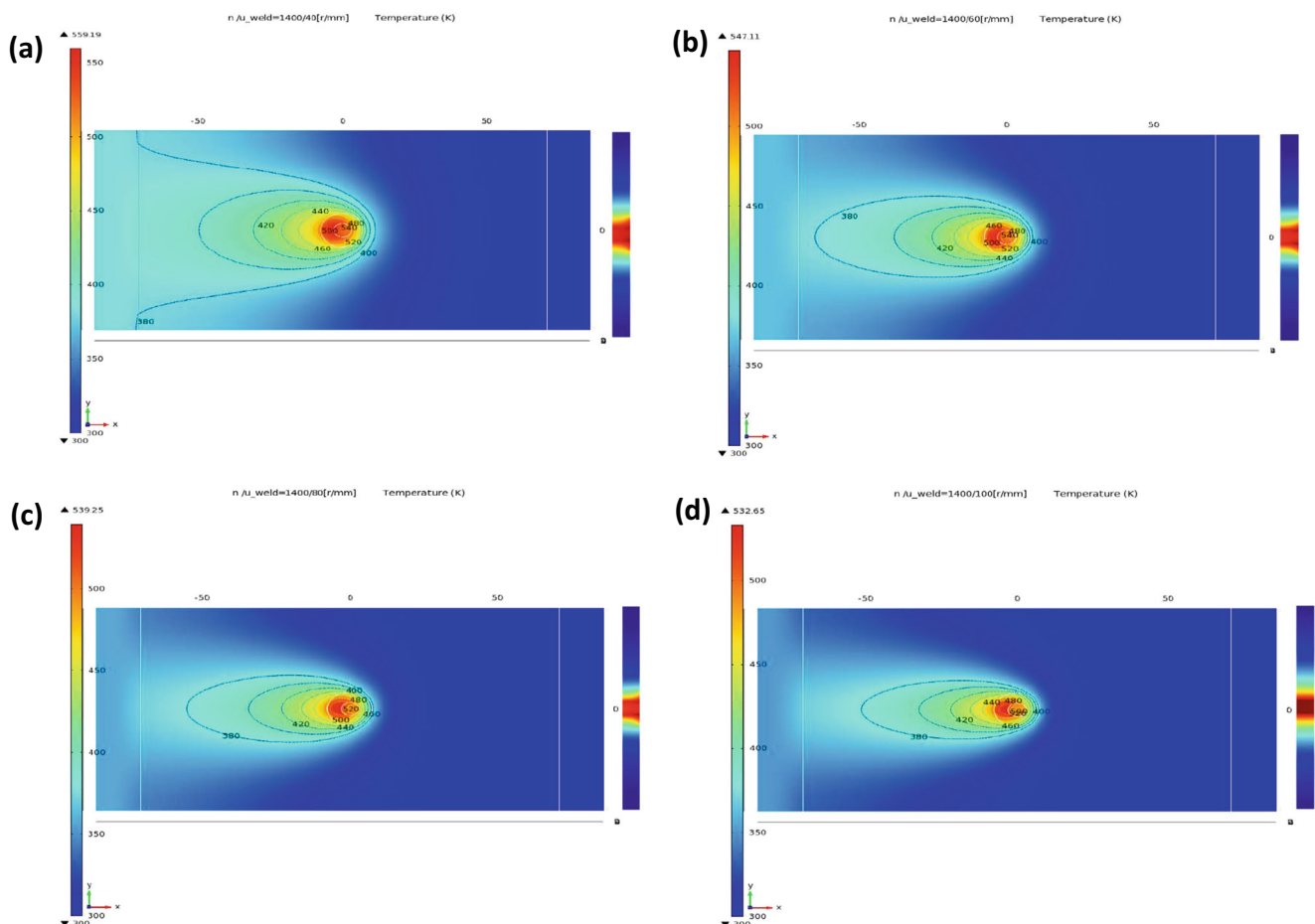


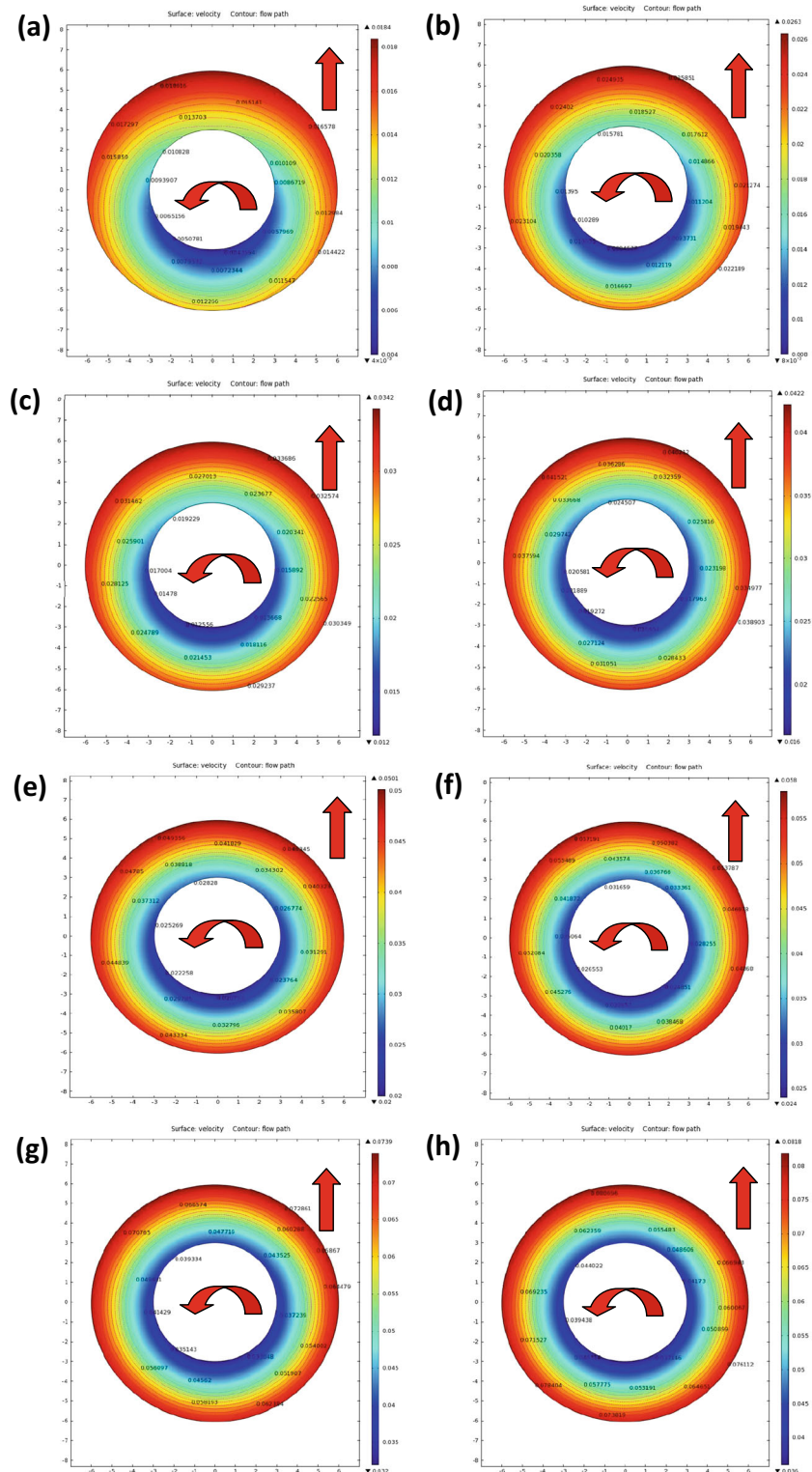
Fig. 8 Isothermal contour of temperature field (*left*) and weld shape (*right*) under R_w/U_w of **a** 1400/40, **b** 1400/60, **c** 1400/80, and **d** 1400/100 r/mm

in insufficient heat input or deficient material flow during the FSW process. The simulation results in the present study show that the groove defects were prone to generate when R_{ω}/U_w was very low or very high, because high welding speed or low

rotational speed might lead to insufficient heat input or deficient material flow.

The interval of surface stripes and curvature of arch lines can be predicted by the coupled model in this paper. Figure 9

Fig. 9 Flow paths of the material element and velocity isoline image under the ratio $\delta R_{\omega}/U_w$ of **a** 0.4, **b** 0.6, **c** 0.8, **d** 1, **e** 1.2, **f** 1.4, **g** 1.6, and **h** 1.8. (Red arrows stand for welding and rotational direction)

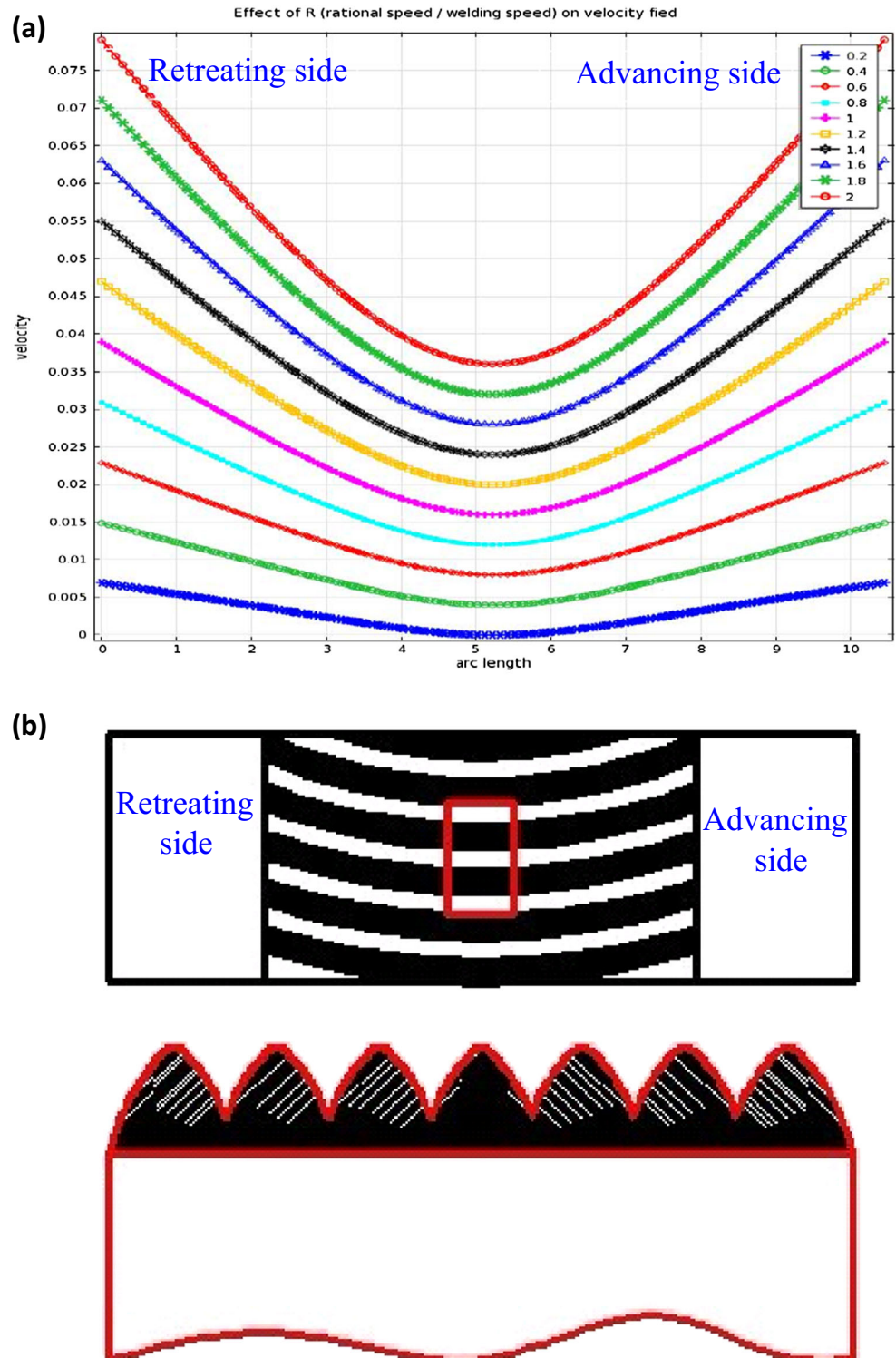


shows the interval of surface stripes and curvature of arch lines when the ratio $\delta \cdot R_{\omega}/U_w$ was 0.6.

The calculated average radius of curvature of arch lines was 8.9 mm, while the measured value was 7.6 mm. The

calculated average interval of surface stripes was 0.48 mm, while the measured value was 0.42 mm. It suggests that the coupled model can predict the interval of surface stripes and curvature of arch lines.

Fig. 10 Stripes of velocity field and surface ribbon textures in the SAZ with the increase of the ratio $\delta \cdot R_{\omega}/U_w$: **a** stripes of velocity field; **b** surface ribbon textures ($\delta \cdot R_{\omega}/U_w = 0.6$)



4 Results and discussion

The welding parameters used in the simulation are shown in Table 2. The welding speed ranged from 20 to 100 mm/min with an increment of 20 mm/min and from 100 to 700 mm/min with an increment of 100 mm/min.

4.1 Effect of R_{ω/U_w} on temperature field

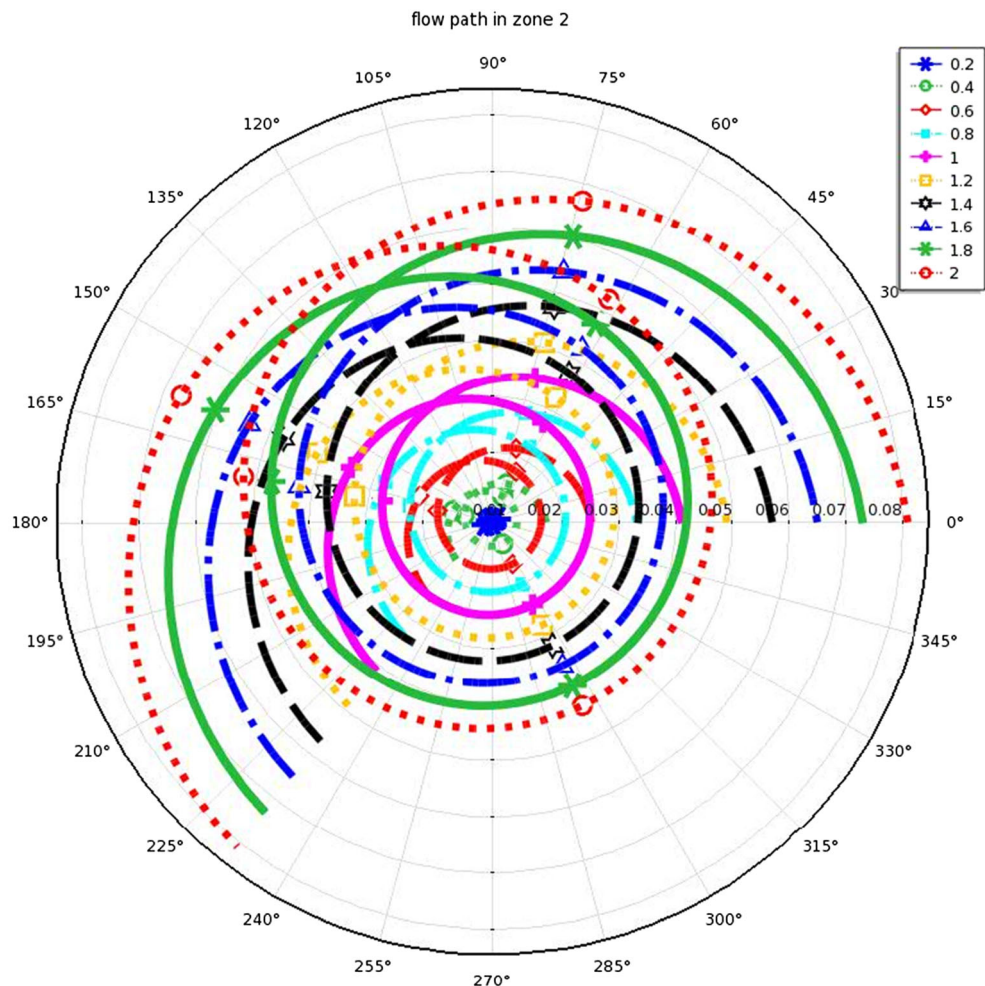
The increase of welding speed/rotational speed ratio R_{ω/U_w} resulted in the increase of the temperature gradients around the pin and the weld width. This result was attributed to the variation of heat input, which caused the change of cooling rate. The heat-affected zone (HAZ) became wider as R_{ω/U_w} increased. When R_{ω/U_w} was 1400/40 r/mm (Fig. 8a), there was a high temperature and a low thermal gradient in the HAZ. Smallest HAZ formed when R_{ω/U_w} was 1400/100 r/mm (Fig. 8d), and the joint had a rectangular-shaped weld. When R_{ω/U_w} was too small, the tunnel defect occurred in the weld. The welded joint had an insufficient heat input which is

caused by the increase of welding speed and will lead to poor plasticization of the base metal and affects the flow behavior of the material. The isothermal contours and HAZ range under the ratio R_{ω/U_w} of 1400/60 r/mm (Fig. 8b) showed the best temperature distribution, and the weld had a shape similar to an isosceles trapezoid, which could enhance the strength of the weld joints. The temperature distribution in the vicinity of the pin transformed from non-uniform to uniform as R_{ω/U_w} increased. The peak temperature only appeared initially at the back of shoulder-affected zone (SAZ) and had a larger range as R_{ω/U_w} increased.

4.2 Effect of R_{ω/U_w} on the flow field

Based on kinematical analytical equations, the welding speed and the rotational speed in FSW have significant influence on the velocity field of welded material. The effects of R_{ω/U_w} on material flow were studied in Rajakumar et al. [23–26]. To conveniently describe the effects of ratio R_{ω/U_w} on material flow, the spatial variable, fractional slip δ , at the workpiece/

Fig. 11 Flow paths under different ratios of $\delta \cdot R_{\omega/U_w}$



tool interface was used for the relationship between the tool rotational speed and the material rotational speed around the tool:

$$\omega_m = \delta \cdot \omega_{\text{tool}} \quad (17)$$

where ω_m is the material rotational speed around the tool, and ω_{tool} is the tool rotational speed.

R_{ω/U_w} can be replaced by $\delta \cdot R_{\omega/U_w}$. Figure 9 illustrates the effects of rotational speed on material flow and velocity field in the SAZ (zone 1, as shown in Fig. 2) under a welding speed of 60 mm/min. Figure 9 shows the flow paths of the material element and velocity isoline image when the ratio $\delta \cdot R_{\omega/U_w}$ varied from 0.4 to 1.8 with the increment of 0.2. The material flow velocity increased with the increase of the rotational speed in the SAZ. Thus, the material flow velocity is also a function of $\delta \cdot R_{\omega/U_w}$.

The flow path in Fig. 9a shows an eccentric circle-shaped relative to the pin of the tool. The flow path became more concentric circular shaped with the increase of the ratio $\delta \cdot R_{\omega/U_w}$ (as shown in Fig. 9d). The tangent velocity of the material flow (i.e., circumferential velocity) played a leading role

in the entire flow field under a high rotational velocity (as shown in Fig. 9g).

The surface ribbon texture in the SAZ is responsible for the formation of surface morphology of the joint, as described by Fig. 10. Figure 10a shows that the maximum velocity magnitude in SAZ appeared in the front of the retreating side (RS), and the minimum velocity magnitude appeared in the rear of the RS. The velocity at the RS was slightly higher than that at the advancing side (AS) at the same distance from the center of the pin. The velocity of the material flow at the outer sides of SAZ was higher than that in the center of SAZ. The above results are in agreement with the results observed by Morisada et al. [27] using the X-ray transmission system. Figure 10a also clearly describes the effect of the ratio $\delta \cdot R_{\omega/U_w}$ on the velocity field. It can be concluded that the evolution process of velocity field was affected by the change of the ratio $\delta \cdot R_{\omega/U_w}$, and the stripe of the velocity field in the SAZ coincided with surface ribbon texture in the SAZ, as shown in Fig. 10b.

The dependency of the velocity field on the ratio $\delta \cdot R_{\omega/U_w}$ was achieved by the parametric sweep function based on the FEM method. The effect of process parameters on the mixing pattern was investigated quantitatively by means of the batch

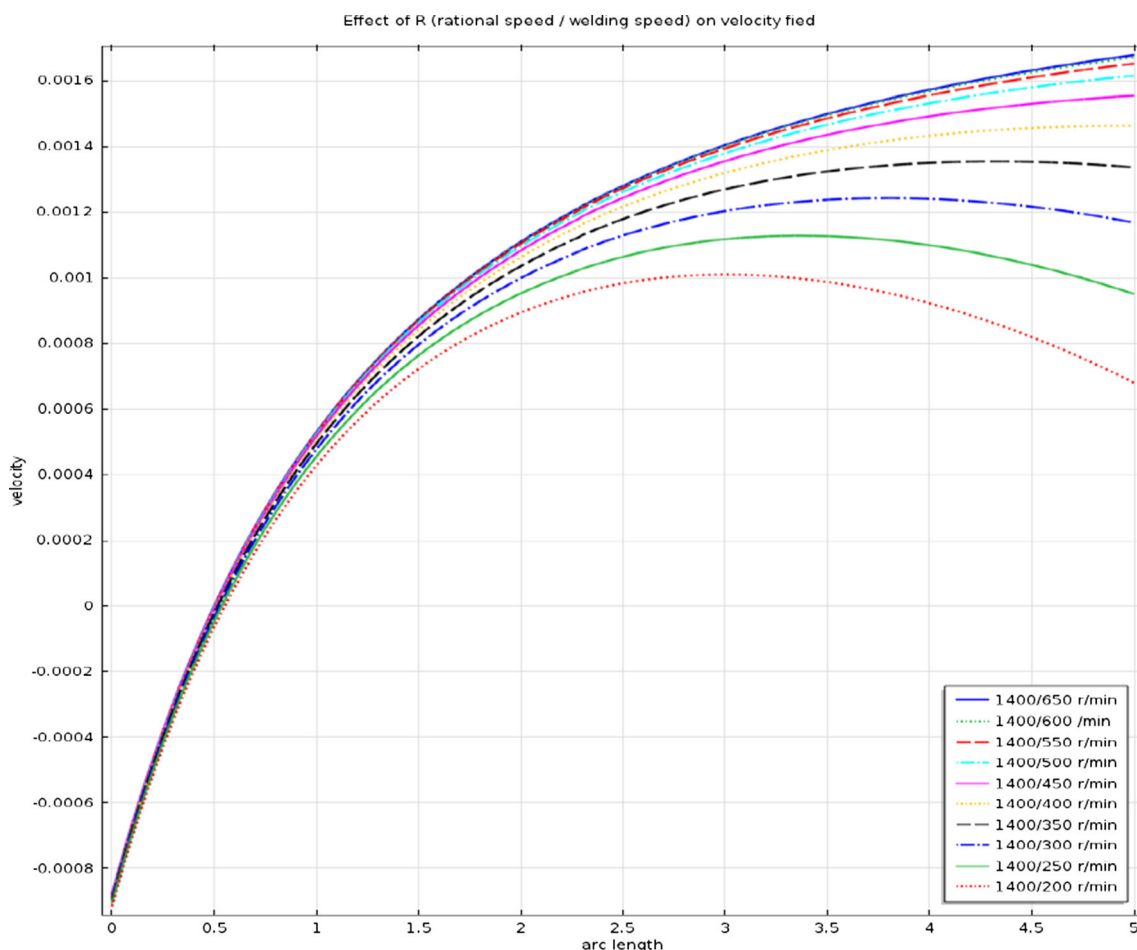


Fig. 12 Flow velocity at SAZ with the change of R_{ω/U_w}

processing mode in the simulation process. Figure 11 indicates that flow paths were around the center of the “nugget zone” (zone 2 shown in Fig. 2) in the XOY plane, and formed a vortex. In Fig. 11, the flow velocity of material increased with the increase of $\delta \cdot R_{\omega/U_w}$. All the curves were cut off at the rear of RS. These flow paths show the beginning or termination and the up or down movement of materials. Moreover, the ratio $\delta \cdot R_{\omega/U_w}$ had no effect on the flow tendency of materials. Figure 11 is in agreement with the conclusions obtained by Zhang et al. [28].

Figure 12 shows material flow velocity of SAZ in FSW with the change of ratio R_{ω/U_w} from 1400/650 to 1400/200 r/mm. In the SAZ, the material flow rate gradually decreased as the ratio R_{ω/U_w} increased. The radius of curvature increased with the decrease of R_{ω/U_w} . The center of curvature gradually moved towards the center of the tool as R_{ω/U_w} decreased. When R_{ω/U_w} reached 1400/650 r/mm, the coordinate radius of measurement points in the SAZ indicates the radius of material flow in FSW, Fig. 12 can be used to predict the track of material flow during FSW.

5 Conclusions

- Compared with the pure CFD or FEM model, the FEM and SAM combination method has significant benefits to deal with the strong nonlinear question. The model was successful in making predictions including weld shape, surface stripes interval, curvature of arch lines, weld defect, and peak temperature R_{ω/U_w} .
- The groove defect was prone to generate when was either very low or very high.
- The experimental results agreed well with the simulation results under different welding parameters. The multiphysics coupled model was proven to be valid and reliable.
- The temperature gradients around the pin and the weld width increased and temperature distribution around the pin had a tendency of transforming from non-uniform to uniform as the rotational speed to welding speed ratio R_{ω/U_w} increased. The peak temperature only appeared initially at the back of SAZ and had a larger range as R_{ω/U_w} increased.
- The material flow paths changed from an eccentric circle shape to a concentric circle shape with the increase of the ratio $\delta \cdot R_{\omega/U_w}$. The surface ribbon texture in the SAZ was responsible for the formation of surface morphology under the effect of the ratio $\delta \cdot R_{\omega/U_w}$. The curves were around the center of the “nugget zone” and formed a vortex. In the SAZ, the material flow rate gradually decreased as increased.

Acknowledgments The authors gratefully acknowledge the support from the Natural Science Foundation of China (No.51075413), Excellent Talents Project in Universities of Chongqing Municipal Education Commission, People’s Republic of China. The authors would like to thank Assistant Professor Dr. Liu Qinzong at the Sam Houston State University in USA for helpful discussion.

References

1. Nandan R, DebRoy T, Bhadeshia HKDH (2008) Recent advances in friction-stir welding—process, weldment structure and properties. *Prog Mater Sci* 53:980–1023
2. Cam G (2011) Friction stir welded structural materials: beyond Al-alloys. *Int Mater Rev* 56:1–48
3. Cam G, Mistikoglu S (2014) Recent developments in friction stir welding of Al-alloys. *J Mater Eng Perform* 23:1936–1953
4. Schmidt H, Hattel J (2005) A local model for the thermo-mechanical conditions in friction stir welding. *Model Simul Mater Sci Eng* 13:77–93
5. Sonne MR, Tutum CC, Hattel JH, Simar A, de Meester B (2013) The effect of hardening laws and thermal softening on modeling residual stresses in FSW of aluminum alloy 2024-T3. *J Mater Process Technol* 213:477–486
6. Carlone P, Palazzo GS (2013) Influence of process parameters on microstructure and mechanical properties in AA2024-T3 friction stir welding. *Metall Microstruct Anal* 2:213–222
7. Smith CB, Bendzsak GB, North TH, Hinrichs JF, Noruk JS, Heideman RJ (2000) Heat and material flow modeling of the friction stir welding process. *Proc Ninth Int Conf Computer Technol Weld.*, Detroit, MI, USA
8. Ulysse P (2002) Three-dimensional modeling of the friction stir welding process. *Int J Mach Tools Manuf* 42:1549–1557
9. Deng XM, Xu SW (2004) Two-dimensional finite element simulation of material flow in the friction stir welding process. *Int J Mach Tools Manuf* 6:125–133
10. Colegrove PA, Shercliff HR (2005) Three-dimensional CFD modelling of flow round a threaded friction stir welding tool profile. *J Mater Proc Technol* 169:320–327
11. Heurtier P, Jones MJ, Desrayaud C, Driver JH, Montheillet F, Allehaux D (2006) Mechanical and thermal modelling of friction stir welding. *J Mater Proc Technol* 171:348–357
12. Zhang HW, Zhang Z, Chen JT (2007) 3D modeling of material flow in friction stir welding under different process parameters. *J Mater Proc Technol* 183:62–70
13. Nandan R, Roy GG, Lienert TJ, Debroy T (2007) Three-dimensional heat and material flow during friction stir welding of mild steel. *Acta Mater* 55:883–895
14. Jacquin D, De Meester B, Simar A, Deloison D, Montheillet F, Desrayaud C (2011) A simple Eulerian thermomechanical modeling of friction stir welding. *J Mater Proc Technol* 211:57–65
15. Zhang ZH, Li WY, Li JL et al (2014) Effective predictions of ultimate tensile strength, peak temperature and grain size of friction stir welded AA2024 alloy joints. *Int J Adv Manuf Technol* 73:1213–1218
16. Zhang Z, Zhang HW (2014) Solid mechanics-based Eulerian model of friction stir welding. *Int J Adv Manuf Technol* 72:1647–1653
17. Al-Badour F, Merah N, Shuaib A et al (2014) Thermo-mechanical finite element model of friction stir welding of dissimilar alloys. *Int J Adv Manuf Technol* 72:607–617
18. Buffa G, Hua J, Shivpuri R, Fratini L (2006) A continuum based fem model for friction stir welding-model development. *Mater Sci Eng A* 419:389–396

19. Zhang XX, Xiao BL, Ma ZY (2011) A transient thermal model for friction stir weld. *Metall Mater Trans A* 42:3218–3228
20. Song M, Kovacevic R (2003) Thermal modeling of friction stir welding in a moving coordinate system and its validation. *Int J Mach Tools Manuf* 43:605–615
21. Lin BY, Yuan P, Liu JJ (2011) Temperature distribution of aluminium alloys under friction stir welding. *Adv Mater Res* 264–265: 217–222
22. Wang L, Xie LY (2011) Measurement and analysis of temperature in friction stirring welding process. *Light Alloy Fabr Technol* 39: 54–59
23. Rajakumar S, Muralidharan C, Balasubramanian V (2010) Influence of friction stir welding process and tool parameters on strength properties of AA7075-T6 aluminium alloy joints. *Mater Des* 32:535–549
24. Rajakumar S, Muralidharan C, Balasubramanian V (2010) Establishing empirical relationships to predict grain size and tensile strength of friction stir welded AA 6061-T6 aluminium alloy joints. *Trans Nonferrous Metals Soc China* 20:1863–1872
25. Rajakumar S, Muralidharan C, Balasubramanian V (2011) Predicting tensile strength, hardness and corrosion rate of friction stir welded AA6061-T6 aluminium alloy joints. *Mater Des* 32: 2878–2890
26. Rajakumar S, Balasubramanian V (2012) Correlation between weld nugget grain size, weld nugget hardness and tensile strength of friction stir welded commercial grade aluminium alloy joints. *Mater Des* 34:242–251
27. Morisada Y, Fujii H, Kawahito Y, Nakata K, Tanaka M (2011) Three-dimensional visualization of material flow during friction stir welding by two pairs of X-ray transmission systems. *Scripta Mater* 65:1085–1088
28. Zhang HW, Zhang Z, Chen JT (2005) Effect of angular velocity of the pin on material flow during friction stir welding. *Acta Metall Sin* 41:853–859